Multicluster and traveling chimera states in nonlocal phase-coupled oscillators

Jianbo Xie* and Edgar Knobloch†
Department of Physics, University of California at Berkeley, Berkeley, California 94720, USA

Hsien-Ching Kao‡
Wolfram Research Inc., Champaign, Illinois 61820, USA
(Received 14 April 2014; published 29 August 2014)

Chimera states consisting of domains of coherently and incoherently oscillating identical oscillators with nonlocal coupling are studied. These states usually coexist with the fully synchronized state and have a small basin of attraction. We propose a nonlocal phase-coupled model in which chimera states develop from random initial conditions. Several classes of chimera states have been found: (a) stationary multicluster states with evenly distributed coherent clusters, (b) stationary multicluster states with unevenly distributed clusters, and (c) a single cluster state traveling with a constant speed across the system. Traveling coherent states are also identified. A self-consistent continuum description of these states is provided and their stability properties analyzed through a combination of linear stability analysis and numerical simulation.

DOI: 10.1103/PhysRevE.90.022919 PACS number(s): 05.45.−a, 89.75.Kd

I. INTRODUCTION

Networks of coupled oscillators have been studied extensively for many years, motivated by a wide range of applications in physics, chemistry, and biology [1,2]. Examples include laser arrays [3], coupled Josephson junctions [4], firefly populations [5], etc. When the coupling is weak, changes in the oscillation amplitude can be neglected and the oscillator system can be reduced, by means of phase reduction [6], to a system of phase-coupled oscillators. Among the models of phase-coupled oscillators, Kuramoto-type models [7–9] are best known. In these models, each oscillator is described by a single phase variable θ which interacts with the others through a sinusoidal coupling. Many efforts have been made to describe the dynamics that prevail when the coupling is either local or global [9–11], but the effects of nonlocal coupling remain relatively unexplored. Kuramoto and Battogtokh [12] investigated a system of identical oscillators, each with natural frequency ω, described in the continuum limit by the equation

$$\frac{\partial\theta}{\partial t} = \omega - \int G(x-y)\sin[\theta(x,t) - \theta(y,t) + \alpha]\,dy \quad (1)$$

and discovered, for the coupling function $G(y) = \frac{\kappa}{2}\exp(-\kappa|y|)$, states of partial synchronization. These states, called chimera states [13], consist of a domain or domains of coherent, phase-locked oscillators embedded in a background of incoherent oscillators, and resemble states consisting of laminar flow embedded within a turbulent state familiar from studies of plane Couette flow [14–16].

To obtain chimera states within the system (1) two basic conditions must be satisfied [17]: the coupling must be nonlocal and the parameter α must be nonzero. In fact, the chimera states are mostly found when $\alpha \approx \frac{\pi}{2}$. These numerical observations inform many of the subsequent studies of the chimera state [18–25]. In these papers, the coupling function $G(x)$ is chosen to be a nonnegative even function that decreases monotonically with $|x|$. In the present paper, we retain the property that $G(x)$ is even but relax, following Ref. [25], both the monotonicity requirement and the requirement that it be nonnegative. Our motivation for this generalization of the coupled oscillator problem comes from biology, and in particular neural systems [26], in which negative coupling at large separations is quite typical. With this coupling, we have found a much richer variety of chimera states, including a remarkable traveling chimera state. Some of these states, such as multicluster chimera states, are similar to those reported recently in Refs. [19,23,24]. Of these Ref. [19] reports the presence of multicluster chimera states in a particular time-delay system, while Refs. [23] and [24] report a two-cluster state and an evenly spaced multicluster state, respectively. However, no analytical description of these states or of their stability properties is provided.

We consider phase oscillators distributed uniformly on a one-dimensional ring of length 2π. The value of ω can be set to zero by going into a rotating frame. The model equation then takes the form

$$\frac{\partial\theta}{\partial t} = -\int_{-\pi}^{\pi} G(x-y)\sin[\theta(x,t) - \theta(y,t) + \alpha]\,dy \quad (2)$$

with $\alpha \in [0,\pi/2]$. For later convenience, we define $\beta \equiv \frac{\pi}{2} - \alpha$. Two families of coupling functions are considered:

$$G_n^{(1)}(x) \equiv \cos(nx), \quad G_n^{(2)}(x) \equiv \cos(nx) + \cos[(n+1)x],$$

where n is an arbitrary positive integer. In each case the coefficient in front of the coupling function has been set equal to unity by rescaling time. In both cases, if $\theta(x,t)$ is a solution so is $\theta(-x,t)$. In view of the periodic boundary conditions this implies that Eq. (2) possesses $O(2)$ symmetry [8]. In particular we are guaranteed the presence of reflection-symmetric solutions; such solutions cannot drift in the x direction, and we refer to them as stationary states or standing waves. On the other hand solutions that break the symmetry $x \to -x$ are expected to drift in the x direction, and we refer to such solutions as traveling waves; for each solution that drifts

*swordwave@berkeley.edu
†knobloch@berkeley.edu
‡hkao@wolfram.com

 ©2014 American Physical Society

to the right there is a solution that drifts to the left, obtained by reflection in x.

The approach we follow is closest to that of Omel'chenko [25] who proved a number of general results about Eq. (2) for general coupling functions $G(x)$, while focusing on two simple choices, $G(x) = (2\pi)^{-1}(1 + A\cos x)$, $0 < A < 1$ [13,17], and $G(x) = (2\pi r)^{-1}$ for $|x| \leqslant \pi r$ and zero otherwise [21,27]. Our results for $G_n^{(1)}(x)$ resemble known results for $G(x) = (2\pi)^{-1}(1 + A\cos x)$, $0 < A < 1$, in that we identify both single and multicluster chimeras with evenly distributed clusters, indicating that the nonzero mean of $G(x)$ in Ref. [25] does not play a major role. On the other hand the situation changes dramatically when the coupling $G_n^{(2)}(x)$ is used instead. This coupling allows us to identify multicluster chimeras with unevenly distributed clusters as well as two types of traveling structures: a traveling coherent state and a single-cluster traveling chimera state. To characterize these states we solve in each case a nonlinear integral equation for the complex order parameter describing the state in the continuum limit, and compare the result with extensive simulations using large numbers of oscillators that are necessary to reduce the effects of fluctuations due to finite oscillator number. In addition, we follow Ref. [25] in studying the linear stability of these states and examine their bifurcations as the parameter β is varied. Some of these lead to hysteretic transitions to different states, while others lead to nearby stable states.

The paper is organized as follows. In Secs. II and III we study the system (2) with the coupling functions $G_n^{(1)}(x)$ and $G_n^{(2)}(x)$, respectively. In both cases we describe a self-consistency analysis of the chimera states found, focusing on multicluster chimeras and on their stability properties. Section III also reports our results on the two traveling states identified in our numerical simulations with $G_n^{(2)}(x)$ and formulates a nonlinear complex-valued eigenvalue problem for the drift speed and rotation frequency of these states. For the traveling coherent state the solution of this problem is in excellent agreement with the results of numerical simulations despite the episodic nature of the drift near the onset of the drift instability. A brief conclusion is provided in Sec. IV together with directions for future work.

II. $G_n^{(1)}(x)$ COUPLING

In this section, we consider the case $G_n^{(1)}(x) \equiv \cos(nx)$. Here and elsewhere all numerical simulations are performed using a fourth-order Runge-Kutta method with time step $\delta t = 0.025$ and repeated with $\delta t = 0.01$. The ring is discretized into N oscillators with N ranging from 512 to 4096.

A. Splay states

Synchronized states with

$$\theta(x,t) = \Omega t + qx \tag{3}$$

are referred to as splay states [10,11] and form an important class of solutions to both locally and globally coupled phase oscillator systems. In the present context the frequency Ω satisfies

$$\Omega = -\int_{-\pi}^{\pi} G(y)\sin(qy + \alpha)\,dy, \tag{4}$$

and q is an integer in order that periodic boundary conditions be satisfied. States of this type travel with speed $c = -\Omega/q$, i.e., to the right if $\Omega < 0$ and $q > 0$ (positive slope) and to the left if $\Omega < 0$ and $q < 0$ (negative slope) and vice versa if $\Omega > 0$. The fully synchronized state corresponds to the special splay state with $q = 0$ and does not travel. Similar states exist in systems of nonidentical phase oscillators as well [28].

To analyze the linear stability properties of these states, we follow Ref. [11] and let $\theta(x,t) = \Omega t + qx + \eta(x,t)$, where $|\eta| \ll 1$. The linearized equation takes the form

$$\frac{\partial \eta}{\partial t} = \int_{-\pi}^{\pi} G(x-y)\cos[q(x-y) + \alpha][\eta(y,t) - \eta(x,t)]\,dy, \tag{5}$$

which admits solutions of the form $\eta \sim e^{\lambda_m t}e^{imx}$. Here λ_m is the linear growth rate that can be expressed as

$$\lambda_m = \tfrac{1}{2}\left(e^{-i\alpha}\hat{G}_{q+m} + e^{i\alpha}\hat{G}_{q-m}\right) - \hat{G}_q\cos\alpha \tag{6}$$

with $\hat{G}_q \equiv \int_{-\pi}^{\pi} G(y)e^{iqy}\,dy$. This convention is adopted throughout the paper as the definition of a Fourier coefficient. For the coupling function $G_n^{(1)}(x)$, $\hat{G}_q = \pi(\delta_{n+q} + \delta_{n-q})$.

When α is equal to $\frac{\pi}{2}$, all the splay states are marginally stable. With a random incoherent initial condition, the system tends to remain incoherent as time evolves. When $\alpha < \frac{\pi}{2}$, the splay states with $|q| = n$ become linearly stable while all the others become unstable. This is consistent with our numerical simulations. Snapshots of two different stable splay states are shown in Fig. 1. Starting from an unstable splay state with small random noise added or simply from a completely incoherent state with $R = 0$ (see below) we find that the

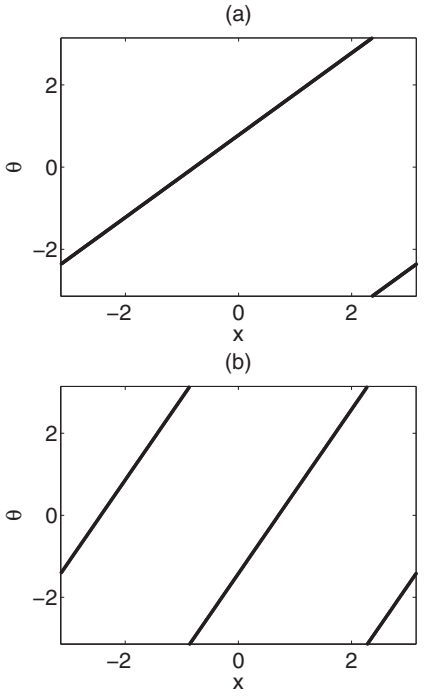

FIG. 1. Stable splay states with (a) $G_1^{(1)}(x) \equiv \cos(x)$ and (b) $G_2^{(1)}(x) \equiv \cos(2x)$. In both cases $\beta = 0.1$ and $N = 512$. State (a) travels with speed $c = 3.124$, while (b) travels with speed $c = 1.563$, both towards the right.

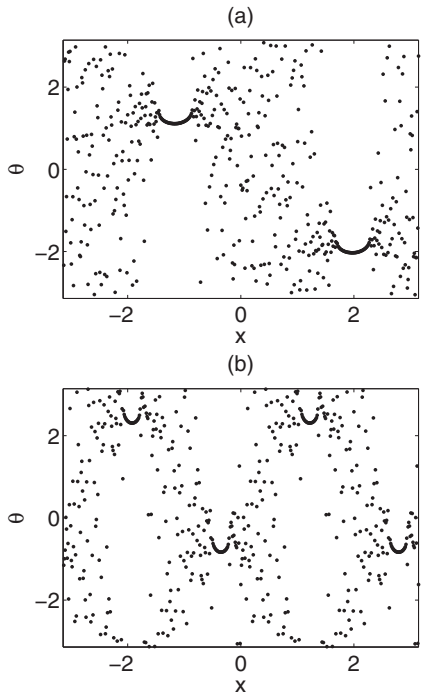

FIG. 2. Chimera states with (a) $G_1^{(1)}(x) \equiv \cos(x)$ and (b) $G_2^{(1)}(x) \equiv \cos(2x)$ obtained from random initial conditions. In both cases $\beta = 0.1$ and $N = 512$.

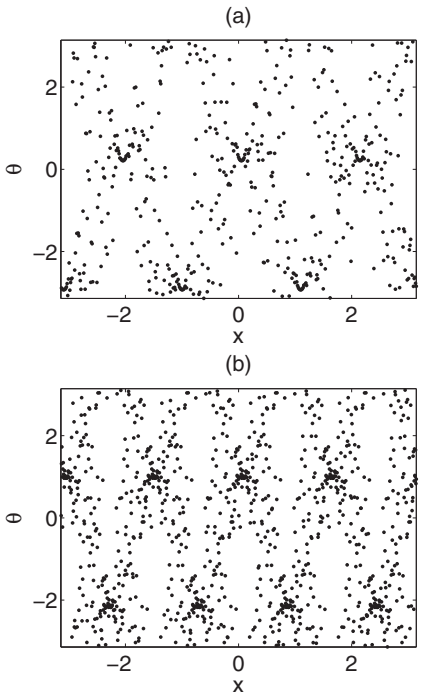

FIG. 3. Chimera states with (a) $G_3^{(1)}(x) \equiv \cos(3x)$ and (b) $G_4^{(1)}(x) \equiv \cos(4x)$ obtained from random initial conditions. (a) $\beta = 0.05$ and $N = 512$; (b) $\beta = 0.02$ and $N = 1024$.

system always evolves into one of two attractors: a stable splay state with $|q| = n$ or a multicluster chimera state. The system is therefore bistable, with the final state selected by the initial condition chosen; cf. Ref. [19]. The properties of the multicluster chimera states are discussed in the next subsection.

B. Multicluster chimera states

As mentioned above, multicluster chimera states are obtained in numerical simulations with the coupling function $G_n^{(1)}(x)$ and different values of n. Figures 2 and 3 show the results for $n = 1, 2, 3$, and 4 and appropriate values of β, all at $t = 5000$. In previous studies [12,13,18], chimera states were observed only when starting from carefully prepared initial conditions while here chimera states are easily obtained even from random initial conditions. This is also the case in a system with nonlinear nonlocal coupling described in Ref. [29]. This suggests the chimera states with the coupling function $G_n^{(1)}(x)$ have a larger basin of attraction than with the exponential coupling function used by Kuramoto and Battogtokh [12]. However, as in the previous studies, chimera states first appear when β is small but nonzero, while for large β the splay state is preferred and appears more and more frequently when the system is initialized using random initial conditions.

The chimeras shown in Figs. 2 and 3 are *stationary* in the sense that they do not display any organized or coherent motion. This is a consequence of the symmetry of these states under spatial reflection. Of course, owing to the incoherence of the surrounding oscillators and their finite number, each coherent cluster will undergo fluctuations in both its location and rotation frequency, although the clusters remain, on average, evenly spaced. These fluctuations are quite small for the simulations reported here and become even smaller as the number N of oscillators increases. Our simulations suggest that the length of the cluster and the positions of the bounding fronts execute zero-mean Brownian motion with standard deviation $\sigma(N)$ (see below).

For $G_n^{(1)}(x) \equiv \cos(nx)$, the number of coherent clusters in the chimera state is always $2n$. In fact, if $\theta(x,t)$ is a solution for $G_1^{(1)}(x)$, then $\theta_m(x,t) \equiv \theta(mx,t)$ is a solution for $G_m^{(1)}(x)$. Thus each multicluster chimera with $G_n^{(1)}(x)$ is in fact a concatenation of n single-cluster chimeras with $G_1^{(1)}(x)$.

To study these chimera states, we proceed as in Ref. [27]. We define a local mean field $z(x,t)$ as the local average of $\exp[i\theta(x,t)]$,

$$z(x,t) \equiv \lim_{\delta\to 0^+} \frac{1}{\delta} \int_{-\delta/2}^{\delta/2} e^{i\theta(x+y,t)}\, dy. \tag{7}$$

The evolution equation for z then takes the form [27,30,31]

$$z_t = \tfrac{1}{2}[e^{-i\alpha} Z(x,t) - z^2 e^{i\alpha} Z^*(x,t)], \tag{8}$$

where $Z(x,t) \equiv Kz(x,t)$ and K is a compact linear operator defined by

$$Kv(x,t) \equiv \int_{-\pi}^{\pi} G(x-y)v(y,t)\, dy. \tag{9}$$

The local mean field $z(x,t)$ effectively smooths out the phase in the incoherent region and yields a well-defined dynamical system.

The chimera states reported above belong to a special class of solutions of Eq. (8) referred to as standing waves [31]. Solutions belonging to this class are stationary in an

appropriate rotating frame. We assume that this frame has angular frequency $-\Omega$ relative to the original frame. In this case the rotating wave takes the form $z(x,t) \equiv e^{-i\Omega t}\tilde{z}(x)$ and Eq. (8) reduces to

$$i\Omega\tilde{z} + \tfrac{1}{2}[e^{-i\alpha}\tilde{Z}(x) - \tilde{z}^2 e^{i\alpha}\tilde{Z}^*(x)] = 0, \tag{10}$$

where $\tilde{Z}(x) \equiv e^{i\Omega t}Z(x,t)$. Solving Eq. (10) as a quadratic equation in $\tilde{z}$ we obtain [27]

$$\tilde{z}(x) = e^{i\beta}\frac{\Omega - \mu(x)}{\tilde{Z}^*(x)} = \frac{e^{i\beta}\tilde{Z}(x)}{\Omega + \mu(x)}, \tag{11}$$

where, for reasons explained in Ref. [27], $\mu(x)$ is equal to $\sqrt{\Omega^2 - |\tilde{Z}(x)|^2}$ when $|\Omega| > |\tilde{Z}(x)|$ and $i\sqrt{|\tilde{Z}(x)|^2 - \Omega^2}$ when $|\Omega| < |\tilde{Z}(x)|$. As explained below this choice of root also corresponds to solutions with a stable essential spectrum and hence to solutions that are potentially stable. Since $\tilde{Z}(x,t) \equiv K\tilde{z}(x,t)$, Eq. (11) is equivalent to the *self-consistency* relation [12]

$$\tilde{Z}(x) \equiv R(x)e^{i\Theta(x)} = \int_{-\pi}^{\pi} G(x-y)e^{i[\beta+\Theta(y)]}h(y)\,dy, \tag{12}$$

where

$$h(x) \equiv \frac{\Omega - \mu(x)}{R(x)} \tag{13}$$

and the x dependence of the quantity μ arises from its dependence on the unknown function $\tilde{Z}(x)$. Here $R > 0$ and Θ are real-valued functions of x and play the role of local order parameters. Equation (12) can be also obtained from the Ott-Antonsen Ansatz [32].

Equation (12) may be applied to our model (Fig. 4). Since Eq. (2) is invariant under (1) translation in x and (2) phase rotation (i.e., translation in θ), it follows that if $R(x)e^{i\Theta(x)}$ is a solution of Eq. (12), then so is $R(x+x_0)e^{i[\Theta(x+x_0)+\Theta_0]}$. Here x_0 and Θ_0 are arbitrary real constants. Using this property, we pick x_0 and Θ_0 such that the self-consistency relation for the $G_n^{(1)}(x)$ coupling takes the form

$$R\exp(i\Theta) = a\cos(nx) + ib\sin(nx), \tag{14}$$

where a and b are real constants satisfying

$$a = e^{i\beta}\langle h(y)e^{i\Theta(y)}\cos(ny)\rangle, \tag{15}$$

$$ib = e^{i\beta}\langle h(y)e^{i\Theta(y)}\sin(ny)\rangle. \tag{16}$$

The bracket $\langle\cdot\rangle$ is defined by $\langle f\rangle = \int_{-\pi}^{\pi} f(y)\,dy$.

This procedure can be applied to the local order parameters $R(x)$ and $\Theta(x)$ shown in Fig. 4(b). Moreover, since both R and Θ are even functions of x with respect to a suitable origin, it follows that $b = 0$ except at phase discontinuities where $R = 0$ [Fig. 4(b)], and hence that $R(x) = R_0|\cos(nx)|$, $R_0 > 0$. The self-consistency relation thus becomes

$$R_0^2 = e^{i\beta}\left\langle\Omega - \sqrt{\Omega^2 - R_0^2\cos^2(ny)}\right\rangle \tag{17}$$

and is independent of n provided n is an integer or a half-integer.

Equation (17) can be regarded as two equations (real and imaginary parts) with two unknowns R_0 and Ω. Solving these equations by numerical continuation with $n = 1$ and $\beta = 0.1$ as the starting point we can determine the dependence of R_0, Ω and the coherent fraction e on β (Fig. 5). The coherent fraction e is defined as the ratio of the total length of coherent clusters to the spatial domain size, 2π. The starting values of R_0 and Ω are first obtained by temporal simulation and then corrected via the self-consistency relation (17). The plots indicate the two-cluster chimera states are born from

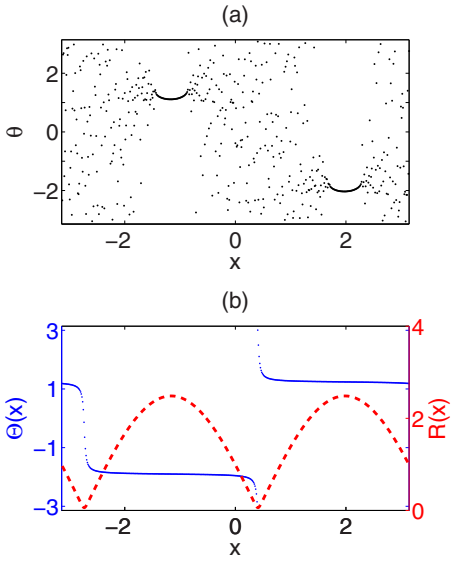

FIG. 4. (Color online) (a) The phase distribution θ in a chimera state with coupling $G_1^{(1)}(x) \equiv \cos(x)$. (b) The local order parameters R (red dashed line) and Θ (blue dotted line) computed from Eq. (7) and the definitions $z(x,t) \equiv e^{-i\Omega t}\tilde{z}(x)$ and $\tilde{Z} \equiv R(x)e^{i\Theta(x)} = K\tilde{z}$. The simulation was done with $\beta = 0.1$ and $N = 512$.

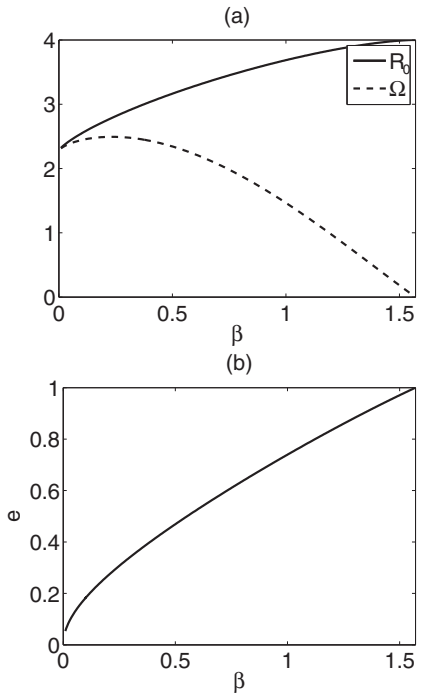

FIG. 5. (a) The quantities R_0 and Ω, and (b) the coherent fraction e, all as functions of β for the two-cluster chimera state with $G_1^{(1)}(x)$ coupling [Fig. 4(a)].

an incoherent state with $R > 0$ as β increases from zero. Even though the self-consistency relation indicates the existence of chimera states for $0 < \beta < \pi/2$, such states are not necessarily stable or have a large enough basin of attraction to be observed in numerical simulations. For example, starting from the two-cluster chimera state in Fig. 4(a), we increased β from 0.1 in small steps, each time evolving the system until it reached a steady chimera solution. This process failed for the first time at $\beta \approx 0.170 \pm 0.005$, where the solution evolved into a $|q| = 1$ splay state. The calculation was repeated with four different choices of N, $N = 512, 1024, 2048$, and 4096, with essentially identical results.

Linear stability of the chimera states can be studied by linearizing Eq. (8) about $\tilde{z}(x)$,

$$v_t = i\mu v + \tfrac{1}{2}[e^{-i\alpha}V - \tilde{z}^2 e^{i\alpha}V^*], \tag{18}$$

where $v(x,t)$ represents a small deviation from $\tilde{z}$ and $V(x,t) \equiv Kv(x,t)$; cf. Ref. [27]. This equation is solved by

$$v(x,t) = e^{\lambda t}v_1(x) + e^{\lambda^* t}v_2^*(x), \tag{19}$$

leading to the eigenvalue problem

$$\lambda \begin{pmatrix} v_1 \\ v_2 \end{pmatrix} = \frac{1}{2}\begin{pmatrix} 2i\mu + e^{-i\alpha}K & -e^{i\alpha}\tilde{z}^2 K \\ -e^{-i\alpha}\tilde{z}^{*2}K & -2i\mu^* + e^{i\alpha}K \end{pmatrix}\begin{pmatrix} v_1 \\ v_2 \end{pmatrix}. \tag{20}$$

Since K is compact [27] (indeed, finite-dimensional for the coupling $G_n^{(1)}$ and $G_n^{(2)}$), its spectrum consists of two parts, a continuous spectrum given by $\{i\mu(x), -i\mu^*(x)\}$ with $x \in [-\pi,\pi)$ and a (possibly empty) point spectrum. The spectrum is in addition symmetric with respect to the real axis: if λ is an eigenvalue with eigenvector $(v_1,v_2)^T$, then λ^* is an eigenvalue with eigenvector $(v_2^*,v_1^*)^T$. The continuous spectrum is stable (negative) or neutrally stable (purely imaginary). Thus the stability of the chimera states is determined by the point spectrum.

We can compute unstable point eigenvalues λ_p numerically. For this purpose we rewrite Eq. (20) in the form

$$\begin{pmatrix} 2 - \frac{e^{-i\alpha}K}{\lambda_p - i\mu} & \frac{e^{i\alpha}\tilde{z}^2 K}{\lambda_p - i\mu} \\ \frac{e^{-i\alpha}\tilde{z}^{*2}K}{\lambda_p + i\mu^*} & 2 - \frac{e^{i\alpha}K}{\lambda_p + i\mu^*} \end{pmatrix}\begin{pmatrix} v_1 \\ v_2 \end{pmatrix} = 0 \tag{21}$$

and define $f \equiv \frac{1}{4}\frac{e^{-i\alpha}}{\lambda_p - i\mu}$, $f^* \equiv \frac{1}{4}\frac{e^{i\alpha}}{\lambda_p + i\mu^*}$, $g \equiv \frac{1}{4}\frac{e^{i\alpha}\tilde{z}^2}{\lambda_p - i\mu}$, and $g^* \equiv \frac{1}{4}\frac{e^{-i\alpha}\tilde{z}^{*2}}{\lambda_p + i\mu^*}$. Note that f^* and g^* are not necessarily the complex conjugate of f and g, as λ_p can be complex. As suggested in Ref. [25], it is convenient to solve the eigenvalue problem using Fourier basis functions, especially so since the coupling function is sinusoidal. Equation (21) then takes the form

$$\sum_m \mathbf{B}_{lm}\hat{\mathbf{v}}_m = 0, \tag{22}$$

where

$$\mathbf{B}_{lm} = \begin{pmatrix} \pi\delta_{l,m} - \hat{f}_{l-m}\hat{G}_m & \hat{g}_{l-m}\hat{G}_m \\ \hat{g}^*_{l-m}\hat{G}_m & \pi\delta_{l,m} - \hat{f}^*_{l-m}\hat{G}_m \end{pmatrix},$$

$$\hat{\mathbf{v}}_m = \begin{pmatrix} \hat{v}_{1,m} \\ \hat{v}_{2,m} \end{pmatrix},$$

and $\hat{f}_l$, $\hat{f}_l^*$, $\hat{g}_l$, $\hat{g}_l^*$ are the Fourier coefficients of f, f^*, g, and g^*, respectively; the latter are defined by $\hat{f}_l = \int_{-\pi}^{\pi} f e^{ilx}dx$, etc.

The point eigenvalue λ_p satisfies the condition $\det(\mathbf{B}(\lambda_p)) = 0$. With the coupling function $G_n^{(1)}$ we obtain

$$\det\begin{pmatrix} 1-\hat{f}_0 & \hat{g}_0 & -\hat{f}_{-2n} & \hat{g}_{-2n} \\ \hat{g}_0^* & 1-\hat{f}_0^* & \hat{g}_{-2n}^* & -\hat{f}_{-2n}^* \\ -\hat{f}_{2n} & \hat{g}_{2n} & 1-\hat{f}_0 & \hat{g}_0 \\ \hat{g}_{2n}^* & -\hat{f}_{2n}^* & \hat{g}_0^* & 1-\hat{f}_0^* \end{pmatrix} = 0, \tag{23}$$

or equivalently

$$w(\lambda) \equiv \det\begin{pmatrix} 1-\hat{f}_0 & -\hat{f}_{-2n} & \hat{g}_0 & \hat{g}_{-2n} \\ -\hat{f}_{2n} & 1-\hat{f}_0 & \hat{g}_{2n} & \hat{g}_0 \\ \hat{g}_0^* & \hat{g}_{-2n}^* & 1-\hat{f}_0^* & -\hat{f}_{-2n}^* \\ \hat{g}_{2n}^* & \hat{g}_0^* & -\hat{f}_{2n}^* & 1-\hat{f}_0^* \end{pmatrix} = 0. \tag{24}$$

The resulting point eigenvalue is computed using continuation based on Newton's method. For the chimera state in Fig. 4(a) the calculation shows that an unstable real point eigenvalue emerges from the continuous spectrum as β increases above $\beta \approx 0.17$, in agreement with the result from direct numerical simulation. To confirm that there is only one unstable point eigenvalue, we evaluate the integral $\frac{1}{2\pi i}\oint w'(\lambda)/w(\lambda)\,d\lambda$ for closed contours in the upper half of the complex λ plane. Since the integral is consistently equal to 1 there are no additional unstable point eigenvalues. Figure 6(a) shows the spectrum of Eq. (20) when $\beta \approx 0.83$, while Fig. 6(b) shows the point eigenvalue λ_p as a function

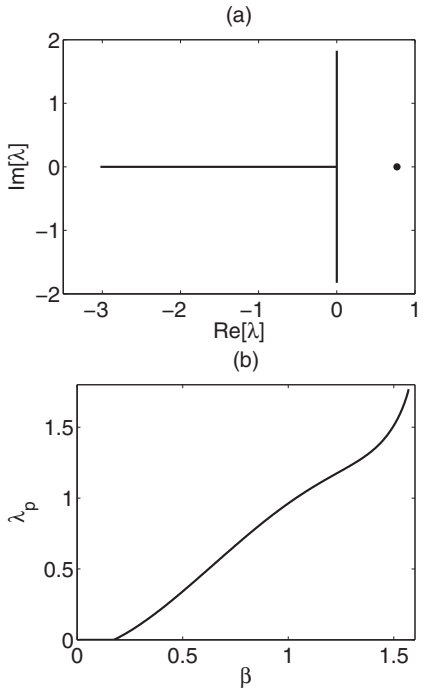

FIG. 6. (a) Spectrum of the linearized operator in Eq. (20) for $G_1^{(1)}$ when $\beta \approx 0.83$. (b) Dependence of the point eigenvalue λ_p on β.

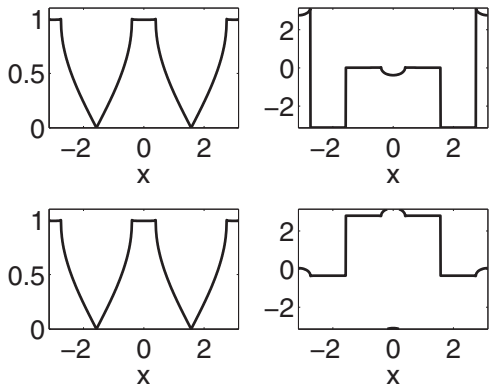

FIG. 7. The eigenvector (v_1, v_2) of the unstable point eigenvalue with coupling $G_1^{(1)}(x)$ at threshold. Left panels: $|v_1(x)|$ and $|v_2(x)|$. Right panels: phase of $v_1(x)$ and $v_2(x)$. The phase jumps by $\pm\pi$ whenever the modulus vanishes.

of β. The corresponding eigenvector is shown in Fig. 7 and is symmetric under reflection $x \to -x$.

As mentioned earlier, owing to the finite number of oscillators in the simulations, each coherent cluster in a multicluster chimera undergoes fluctuations in both its location and rotation frequency, although the clusters remain on average evenly spaced. Here we examine the details of the associated fluctuations numerically for the case $n = 1$ using several different values of N: 256, 362, 512, 724, 1024, 1448, and 2048. For each value of N, we collect data based on time simulation of a two-cluster chimera state starting with three different initial conditions with $R \approx 0$. The total simulation time for each run is 5000. To avoid initial transients, data points between $t = 0$ and 1000 are excluded from the calculation of the statistics.

To obtain the location and rotation frequency of each coherent cluster, we compute the discrete version of the local order parameter $Z^{(N)} \equiv \frac{2\pi}{N} \sum_{m=1}^{N} G(x - x_m) e^{i\theta_m}$, where $x_m = \frac{2\pi m}{N}$ and $\theta_m = \theta(x_m)$, and compare it with the general form of the local order parameter

$$e^{-i\int \Omega\, dt'} \{a \cos[n(x - x_0)] + ib \sin[n(x - x_0)]\} \qquad (25)$$

to obtain the real coefficients x_0, a, b, and Ω, all of which fluctuate as time evolves. Figure 8 shows a sample plot of

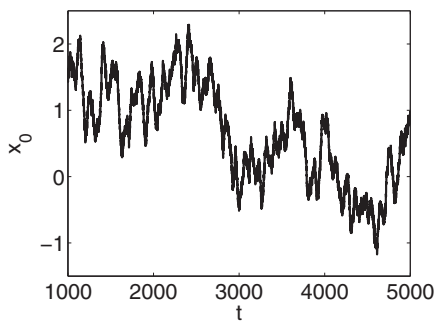

FIG. 8. The position x_0 of a coherent cluster as a function of t in a chimera state obtained with the coupling $G_1^{(1)}(x)$ when $\beta = 0.1$ and $N = 256$.

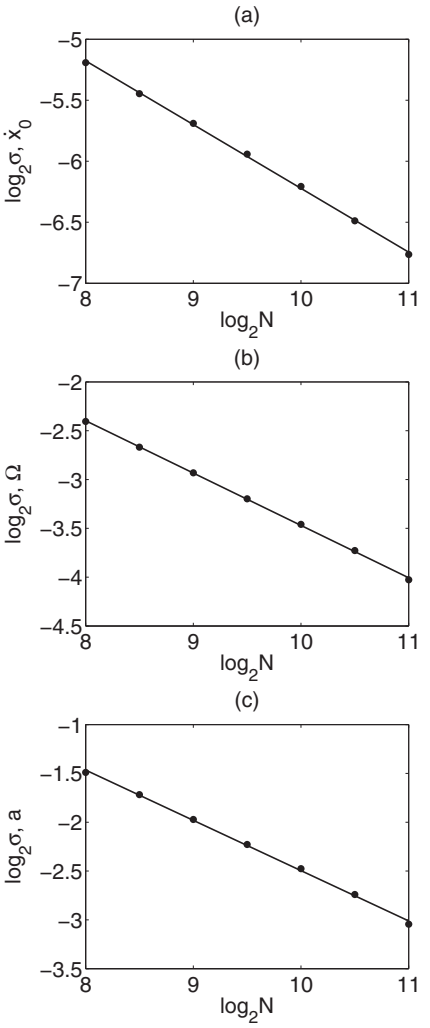

FIG. 9. The dependence of the standard deviation σ of (a) $\dot{x}_0$, (b) $\Omega - \overline{\Omega}$, and (c) $a - \overline{a}$ on $\log_2 N$ when $\beta = 0.1$.

the position x_0 of one of the coherent clusters as a function of t when $\beta = 0.1$ and $N = 256$. Because of the reflection symmetry of this state *on average* we expect the position x_0 to undergo fluctuations with zero mean; cf. Ref. [21].

The dynamics of $\dot{x}_0(t)$, $\Omega(t) - \overline{\Omega}$, and $a(t) - \overline{a}$ are modeled well by a Gaussian white noise $\eta(t)$ satisfying $\overline{\eta(t)\eta(t')} = \sigma^2\delta(t - t')$. Figure 9 shows the dependence of the standard deviation σ on $\log_2 N$ for $\dot{x}_0(t)$, $\Omega(t) - \overline{\Omega}$, and $a(t) - \overline{a}$. The results show that σ scales as $N^{-0.523}$ for $\dot{x}_0$, $N^{-0.536}$ for Ω, and $N^{-0.515}$ for a. For comparison, for a steplike coupling function and a one-cluster chimera the corresponding result is $\sigma \sim N^{-0.845}$ [21].

III. $G_n^{(2)}$ COUPLING

In this section we consider the case with the coupling function $G_n^{(2)}$.

A. Splay states

Splay states with $G_n^{(2)}$ and their linear stability properties are determined as for $G_n^{(1)}$. The growth rate λ_m for an eigenmode

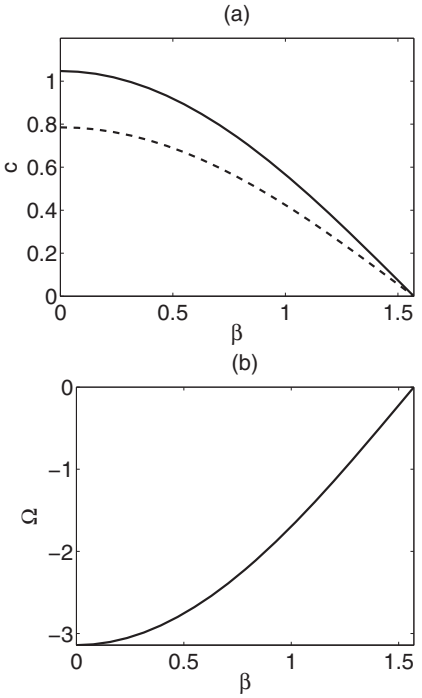

FIG. 10. (a) The dependence of the speed c on β for $n = 3$ (solid line), and $n = 4$ (dashed line) splay states with $G_3^{(2)}$ coupling. (b) The dependence of the frequency Ω on β is the same in both cases.

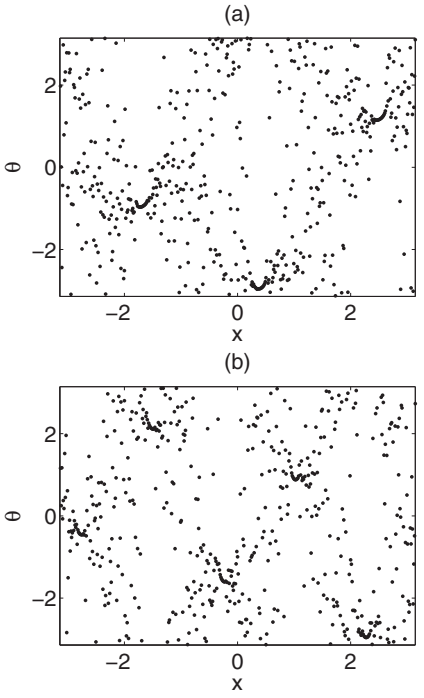

FIG. 11. Chimera states with (a) $G_1^{(2)} \equiv \cos(x) + \cos(2x)$ and (b) $G_2^{(2)} \equiv \cos(2x) + \cos(3x)$ obtained from random initial conditions. In both cases $\beta = 0.03$ and $N = 512$.

of the form e^{imx} still satisfies the relation Eq. (6) but this time with

$$\hat{G}_q = \pi(\delta_{n+q} + \delta_{n-q} + \delta_{n+1+q} + \delta_{n+1-q}). \tag{26}$$

The $|q| = n,\ n+1$ splay states become linearly stable for nonzero β while all the other splay states become unstable. Figure 10 shows the frequency Ω for the stable $n = 3,4$ splay states for $G_3^{(2)}$ coupling as a function of β together with their drift speeds $c = -\Omega/n$. This speed is positive, implying that positive slope splay states travel to the right. As before the final state reached from random initial conditions can be either a splay state with $|q| = n$ or $n+1$, or a stationary multicluster chimera state. However, this time we have also identified a family of entirely new states that can also be reached from random initial conditions: traveling chimera states. Traveling coherent states are also present, as discussed further below.

B. Multicluster chimera states

Here we report our results on stationary multicluster chimera states with the coupling $G_n^{(2)}$. Figures 11 and 12 show the phase distribution in multicluster chimera states obtained with $n = 1$, 2, 3, and 4. The figures reveal a total of $2n+1$ coherent clusters in each case, distributed evenly across both the spatial domain and the phase θ.

We examine the properties of these states in the case $n = 1$. Figure 13 shows the position of one of the coherent clusters as a function of time. The plot indicates that the cluster remains on average stationary, at least for moderate times, although slow drift over very long times cannot be excluded. The apparent stationarity of the cluster permits us to employ a self-consistency analysis analogous to that leading to Eq. (12). With $G = G_1^{(2)}$ this equation yields

$$R\exp(i\Theta) = a\cos x + b\sin x + c\cos(2x) + d\sin(2x), \tag{27}$$

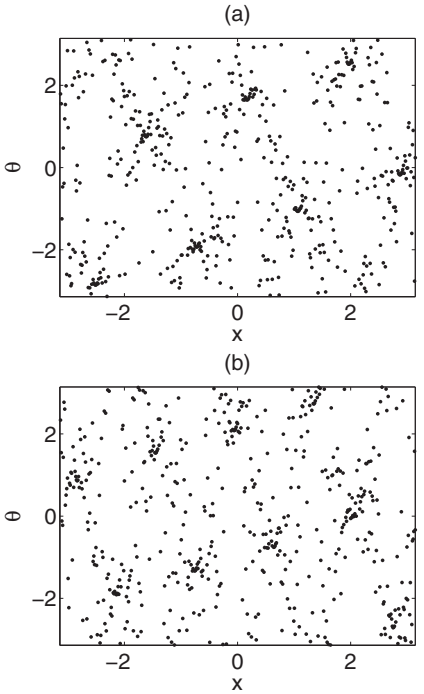

FIG. 12. Chimera states with (a) $G_3^{(2)} \equiv \cos(3x) + \cos(4x)$ and (b) $G_4^{(2)} \equiv \cos(4x) + \cos(5x)$ obtained from random initial conditions. In both cases $\beta = 0.03$ and $N = 512$.

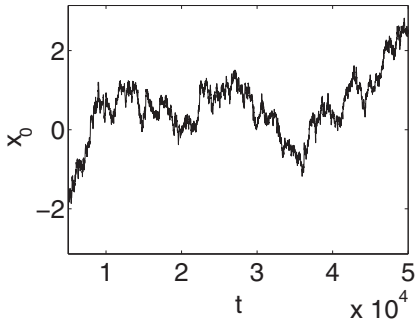

FIG. 13. The position x_0 of a coherent cluster in the three-cluster chimera state obtained with coupling $G_1^{(2)} \equiv \cos(x) + \cos(2x)$ as a function of t for $t \geqslant 5000$ when $\beta = 0.1$ and $N = 512$, starting from random initial conditions at $t = 0$.

where a, b, c, and d are complex numbers given by

$$a = e^{i\beta}\langle h e^{i\Theta} \cos y\rangle,$$
$$b = e^{i\beta}\langle h e^{i\Theta} \sin y\rangle,$$
$$c = e^{i\beta}\langle h e^{i\Theta} \cos 2y\rangle,$$
$$d = e^{i\beta}\langle h e^{i\Theta} \sin 2y\rangle,$$

with h defined as in Eq. (13). Translations in x and θ allow us to fix two of the unknown variables in the self-consistency equation. With these conditions, we can solve for a, b, c, d and the real quantity Ω.

Instead of solving the self-consistency equation by brute force, we observe that Fig. 14 indicates that one can shift the coordinate so that $R(x)$ becomes an even function of x,

$$R(x) = R_0|\cos(3x/2)|, \quad R_0 > 0, \tag{28}$$

while $\Theta(x)$ consists of straight line segments with slope $\pm 1/2$ and phase jumps $\pm\pi$ whenever $R(x)$ touches zero (the case

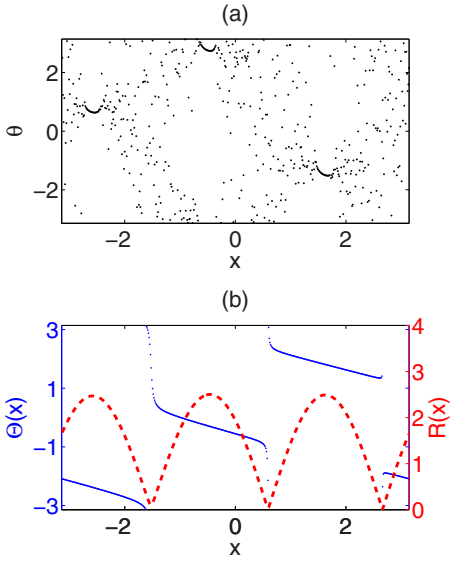

FIG. 14. (Color online) (a) The phase distribution $\theta(x)$ in a three-cluster chimera state with coupling $G_1^{(2)} \equiv \cos(x) + \cos(2x)$ and $\beta = 0.05$, $N = 512$ [Fig. 11(a)]. (b) The local order parameters R (red dashed line) and Θ (blue dotted line).

of positive slope is not shown in Fig. 14 but is also observed in the simulations). The even parity of $R(x)$ is consistent with the observation that the chimera is stationary. Combining these observations with phase translation, we conclude that the local order parameter for the multicluster chimera state takes the form

$$R\exp(i\Theta) = R_0\cos(3x/2)\, e^{\pm ix/2}; \tag{29}$$

indeed, $\tilde{Z}(x) = R_0\cos[(2n+1)x/2]\exp(\pm ix/2)$ for $n \geqslant 1$. Comparing Eq. (29) with Eq. (27), one obtains $a = c = R_0/2$ and $b = -d = \mp i R_0/2$. Substituting Eq. (29) into the self-consistency equation (12) we obtain four relations from the requirement that the coefficients of $\cos x$, $\sin x$, $\cos(2x)$, and $\sin(2x)$ all vanish. It turns out that these relations are all identical, leading to the final self-consistency requirement

$$R_0^2 = e^{i\beta}\left\langle \Omega - \sqrt{\Omega^2 - R_0^2\cos^2(3y/2)}\right\rangle. \tag{30}$$

This equation is of the form (17). Since the solutions of this equation are independent of n when n is an integer or half-integer, the solutions presented in Fig. 5 also describe the β dependence of R_0, Ω and the coherent fraction e for the three-cluster chimera state with $G_1^{(2)}$ coupling. The multicluster chimera states are thus also born from the incoherent state as β increases from zero. Direct numerical simulations show that this time the solution loses stability when β reaches approximately 0.125 ± 0.005, a result obtained with $N = 512$ and confirmed using $N = 1024$ and 2048.

These results are in close agreement with a theoretical stability analysis based on Eq. (22). This time the calculation reveals a pair of unstable complex point eigenvalues that appear as β increases above $\beta \approx 0.120$, followed by an unstable real point eigenvalue that emerges as β reaches $\beta \approx 0.174$ [Fig. 15(b)]. The corresponding eigenvectors are again even (Fig. 16), implying that neither instability results in drift. Numerical contour integration indicates that no other unstable point eigenvalues are present. Figure 15(a) shows the spectrum of Eq. (20) when $\beta \approx 0.83$, while Fig. 15(b) shows the unstable point eigenvalues λ_p as a function of β. The results for $G_3^{(2)}$ are qualitatively similar, with the oscillatory instability appearing at $\beta \approx 0.129$ and the stationary instability located at $\beta \approx 0.176$.

There remains the question whether the multicluster chimera states with the coupling $G_n^{(2)}$ are the only nontrivial solutions of Eq. (12) other than the splay states. Our numerical simulations indicate that the answer is no. Figures 17 and 18 provide two examples of stationary but "exotic" chimera states. Figure 17 shows the results for $G_1^{(2)} \equiv \cos(x) + \cos(2x)$, while Fig. 18 shows the results for $G_2^{(2)} \equiv \cos(2x) + \cos(3x)$, both with $\beta = 0.03$ and $N = 512$. There are several differences between these states and the multicluster chimera states already discussed. First, the number of the clusters is not equal to $2n + 1$. Second, the coherent clusters in these states are distributed nonuniformly in space. As shown in the snapshots, these states consist of two pairs of coherent domains with the components of each pair closer to one another than the mean separation. Finally, the phase of the local order parameter is no longer linear in the spatial variable x and exhibits oscillations. However, we can still shift the x coordinate to make $R(x)$

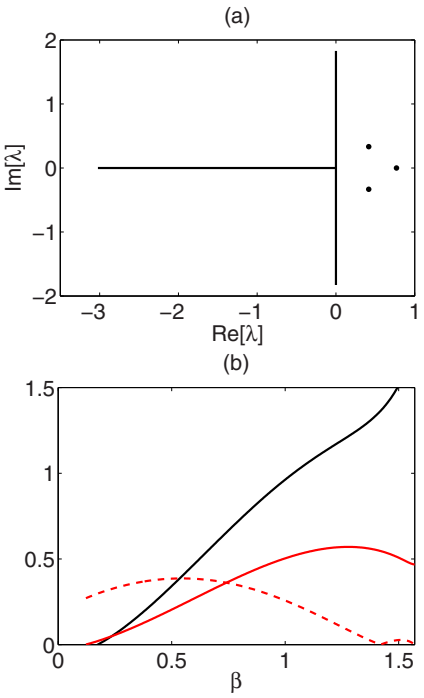

FIG. 15. (Color online) (a) Spectrum of the linearized operator in Eq. (20) for $G_1^{(2)}$ coupling when $\beta \approx 0.83$. (b) Dependence of the point eigenvalues on β. Black line: real point eigenvalue. Red (or gray) solid line: real part of the complex point eigenvalues. Red (or gray) dashed line: imaginary part of the complex point eigenvalues.

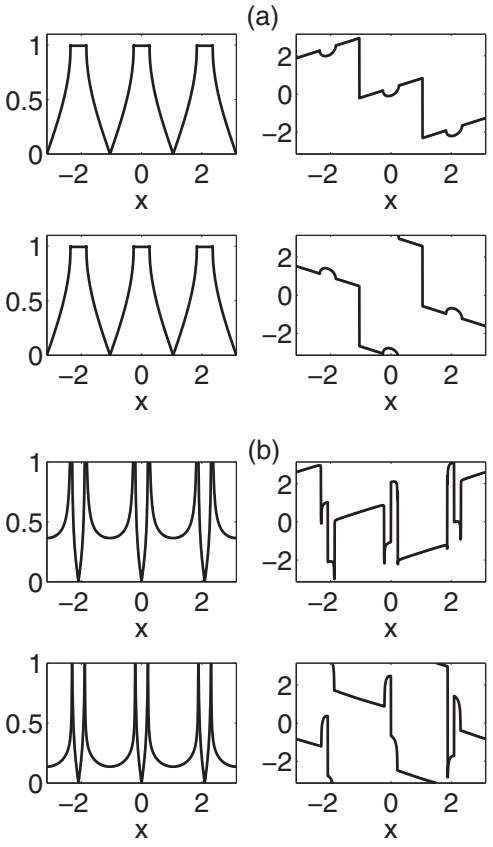

FIG. 16. Eigenvectors of (a) the real unstable mode and (b) the Hopf mode at threshold [Fig. 15(b)]. In each plot, the left panels correspond to $|v_1(x)|$ and $|v_2(x)|$, while the right panels show the phase of $v_1(x)$ and $v_2(x)$. The phase jumps by $\pm\pi$ whenever the modulus vanishes.

even, implying that these exotic chimera states are stationary in space except for an overall rotation frequency Ω (and the presence of fluctuations due to finite size effects).

To understand the properties of the nonuniform multicluster chimera state in Fig. 17 we translate the state such that $R(0) = R(\pi) = 0$. It follows from Eq. (27) that $a = c = 0$, leaving the following two consistency conditions:

$$be^{-i\beta} = \left\langle \frac{b\sin^2 x + d\sin x \sin 2x}{\Omega + \mu(x)} \right\rangle, \tag{31}$$

$$de^{-i\beta} = \left\langle \frac{b\sin x \sin 2x + d\sin^2 2x}{\Omega + \mu(x)} \right\rangle. \tag{32}$$

These equations constitute a pair of complex equations for the complex coefficients b and d and the unknown frequency Ω. However, Fig. 17 also shows that $\Theta(\pi/2) = 0$ (modulo π phase jumps), and we use this observation to deduce that $b_i = 0$. In this case Eqs. (31) and (32) reduce to four real equations for b_r, d_r, d_i, and Ω.

We begin by observing that a solution with order parameter Z for (b_r, d_r, d_i, Ω) implies the presence of a solution with order parameter Z^* for $(b_r, -d_r, -d_i, \Omega)$. This is a consequence of the invariance of the conditions (31)–(32) under $d \to -d$ corresponding to invariance with respect to the translation $x \to x + \pi$. Figure 17 compares a four-cluster chimera state with complex order parameter Z with one with order parameter Z^*, both computed for $\beta = 0.03$. Note also that a solution $\beta, b_r, d_r, d_i, \Omega$ implies the presence of a solution $-\beta, b_r, d_r, -d_i, \Omega$. In view of these symmetries the self-consistency conditions have two solutions for $\beta = 0.03$: $b_r = 2.1985$, $d_r = \mp 0.0073$, $d_i = \pm 1.8375$, $\Omega = 2.4683$. A similar calculation for $G_2^{(2)}$ (Fig. 18) yields the result $b_r = -1.6529$, $d_r = \pm 0.00296$, $d_i = \pm 1.7256$, $\Omega = 2.2426$, again for $\beta = 0.03$. These results agree well with the measured order parameter in both cases.

Having established the value of the self-consistency analysis for the exotic chimera states we now use it as a predictive tool. In Fig. 19 we present a plot of the coefficients (b_r, d_r, d_i, Ω) as a function of the parameter β. The results show that at $\beta \approx 0.24$ the local minima of $R(x)$ touch the line $R = \Omega$ [Fig. 19(b)] and for larger β dip below $R = \Omega$. At this point the quantity $\mu(x)$ in the consistency condition becomes pure imaginary and the solution ceases to exist. We have checked this prediction using numerical simulations. These indicate that for $\beta \gtrsim 0.24$ the four-cluster chimera state indeed disappears and that it does so by a pairwise merger of the clusters, forming a two-cluster chimera for $\beta \gtrsim 0.24$ (Fig. 20).

With increasing β these two remaining clusters gradually grow in length (Fig. 21) but do not merge. Instead this two-cluster state loses stability at $\beta \approx 0.96$ where a real eigenvalue passes through zero. This prediction is consistent with direct numerical simulations provided a sufficiently large number of oscillators is used ($\beta \approx 0.93$ when $N = 512$, $\beta \approx 0.96$ when $N = 2048$). The simulations reveal that this instability is responsible for a strongly hysteretic transition to the stationary

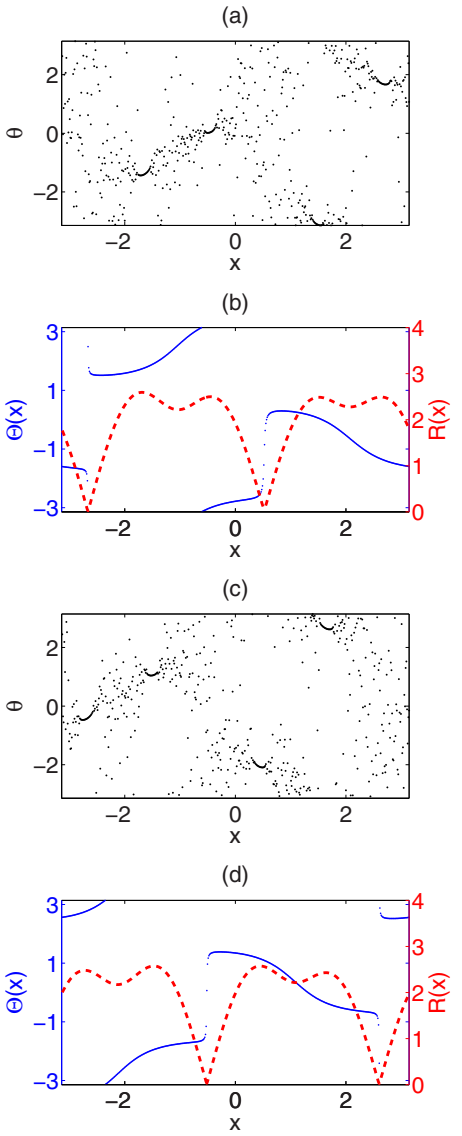

FIG. 17. (Color online) (a) The phase distribution $\theta(x)$ in a four-cluster chimera state with coupling $G_1^{(2)} \equiv \cos(x) + \cos(2x)$ and $\beta = 0.03$, $N = 512$. (b) The local order parameters R (red dashed line) and Θ (blue dotted line). (c, d) A related chimera state with order parameters R and $-\Theta$.

fully coherent state shown in Fig. 22. Since the corresponding order parameters $R(x)$ and $\Theta(x)$ are both even with respect to the same point the coherent state must again be stationary. We therefore write

$$R\exp(i\Theta) = a\cos(x) + c\cos(2x) \tag{33}$$

and use the symmetries of the order parameter to set $a_i = 0$. The self-consistency equations for this case are

$$ae^{-i\beta} = \left\langle \frac{a\cos^2 x + c\cos x\cos 2x}{\Omega + \mu(x)} \right\rangle, \tag{34}$$

$$ce^{-i\beta} = \left\langle \frac{a\cos x\cos 2x + c\cos^2 2x}{\Omega + \mu(x)} \right\rangle. \tag{35}$$

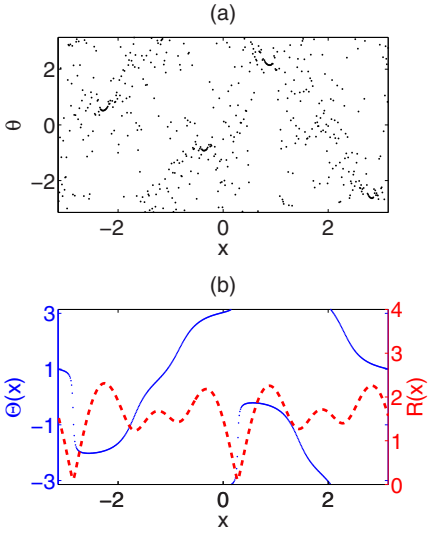

FIG. 18. (Color online) (a) The phase distribution $\theta(x)$ in a four-cluster chimera state with coupling $G_2^{(2)} \equiv \cos(2x) + \cos(3x)$ and $\beta = 0.03$, $N = 512$. (b) The local order parameters R (red dashed line) and Θ (blue dotted line).

Figure 23(a) shows the solution of these equations as a function of β. Solutions exist for all values of β but change their character dramatically below $\beta \approx 0.7644$. Figure 23(b) explains the reason for this change: at this value of β the

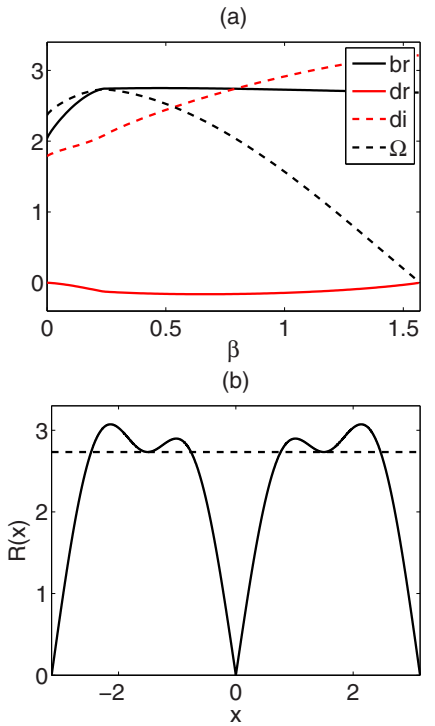

FIG. 19. (Color online) (a) The solution of the self-consistency conditions (31)–(32) as a function of β (b_r: solid black line, d_r: solid red (or gray) line, d_i: dashed red (or gray) line, Ω: dashed black line). (b) The predicted order parameter $R(x)$ at $\beta = 0.24$ (solid line) in comparison with the line $R = \Omega$ (dashed line) indicating that four-cluster chimeras are present for $\beta \lesssim 0.24$; for $\beta \gtrsim 0.24$ only two-cluster chimeras are predicted.

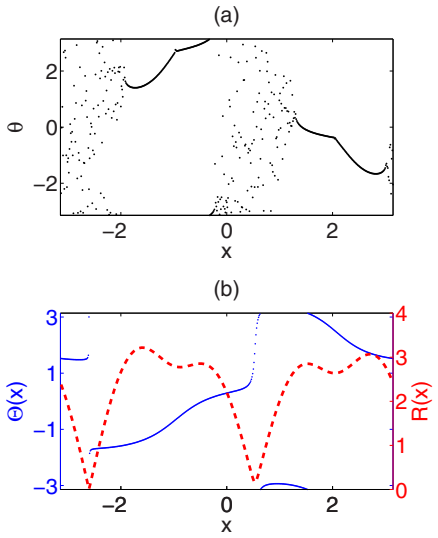

FIG. 20. (Color online) (a) The computed phase distribution $\theta(x)$ at $\beta = 0.24$ and (b) the corresponding order parameter $R(x)$ (red dashed line) and the associated phase $\Theta(x)$ (blue dotted line) for comparison with the prediction in Fig. 19.

global minimum of the order parameter $R(x)$ touches the line $R = \Omega$ for the first time as β decreases, and for $\beta \lesssim 0.7644$ the quantity $\mu(x)$ is no longer everywhere real. However, this time the consequences of this fact are different and are discussed in the next section.

C. Traveling coherent states

Numerical simulations confirm the presence of a stable stationary coherent state for $G_1^{(2)}$ down to $\beta \approx 0.7644$ (a threshold value computed with $N = 512$ oscillators) but reveal

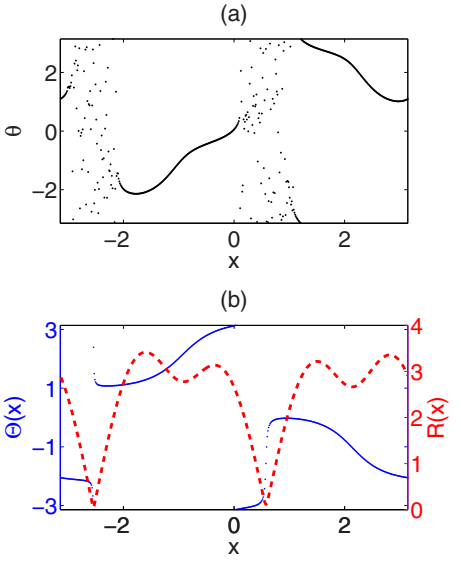

FIG. 21. (Color online) (a) The phase distribution $\theta(x)$ at $\beta = 0.6$ and (b) the corresponding order parameter $R(x)$ (red dashed line) and the associated phase $\Theta(x)$ (blue dotted line) for comparison with Fig. 20.

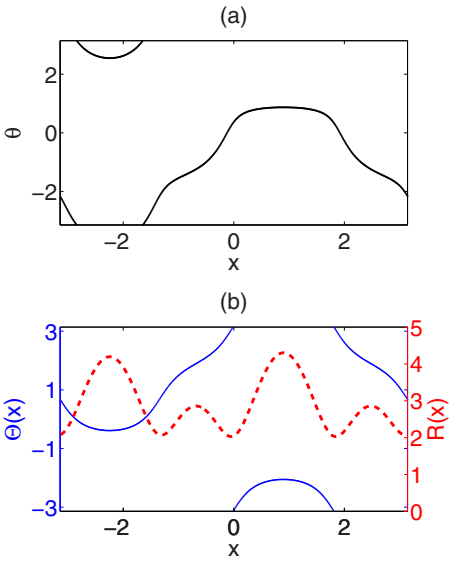

FIG. 22. (Color online) (a) The phase distribution $\theta(x)$ and (b) the corresponding order parameter $R(x)$ (red dashed line) and the associated phase $\Theta(x)$ (blue dotted line) for the stationary coherent state with $G_1^{(2)}$ coupling present at $\beta = 0.96$.

that for lower values of β this state develops a small asymmetry [Fig. 24(b)] and begins to travel to the left. We have examined carefully the behavior of this state near the (nonhysteretic) transition at $\beta \approx 0.7644$. Figure 25(a) shows the position of

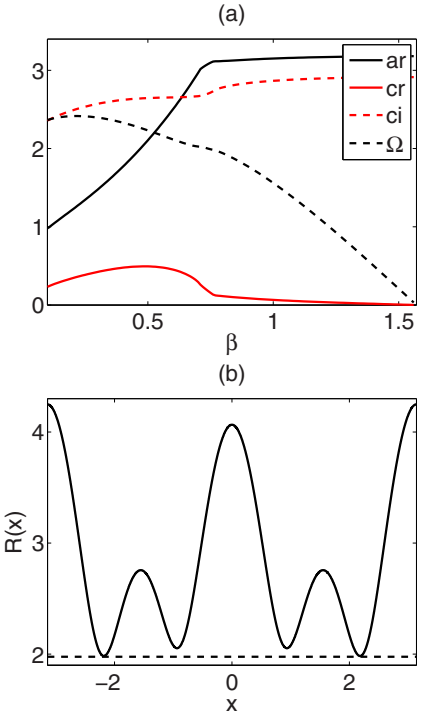

FIG. 23. (Color online) (a) The solution of the self-consistency conditions (34)–(35) as a function of β [a_r: solid black line, c_r: solid red (or gray) line, c_i: dashed red (or gray) line, Ω: dashed black line]. (b) The predicted order parameter $R(x)$ at $\beta = 0.77$ (solid line) in comparison with the line $R = \Omega$ (dashed line).

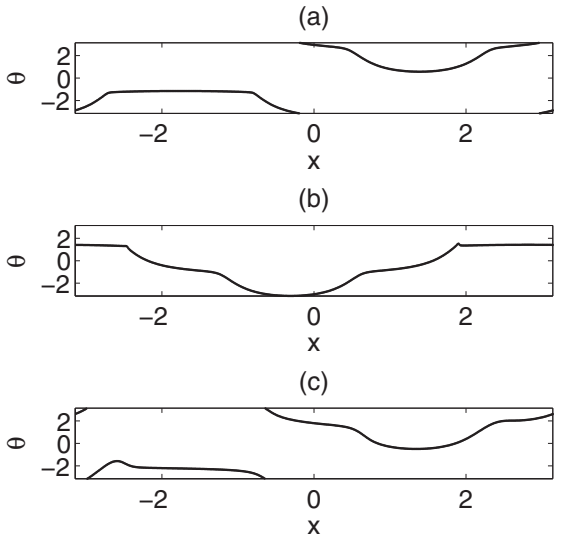

FIG. 24. (a) The phase distribution $\theta(x)$ at (a) $\beta = 0.77$ (symmetric distribution), (b) $\beta = 0.76$ (asymmetric distribution) and (c) $\beta = 0.66$ (asymmetric distribution), all for $N = 512$. The state in (b) oscillates in time while drifting to the left; state (c) travels to the left at constant speed. Reflected solutions travel to the right.

the coherent state as a function of time when $\beta = 0.762$. The figure reveals that the drift speed to the left is not constant in time but is accompanied by small amplitude oscillations. As β increases and one approaches the threshold for this transition the motion takes on the characteristic of stick-slip motion, i.e., the coherent state spends longer and longer periods of time in a near-stationary state, interrupted by brief episodes of slip during which the phase decreases by 2π. In many if not most systems this type of behavior is associated with the presence of a sniper bifurcation, a saddle-node bifurcation of two equilibria on an invariant circle [33]. However, our detailed investigation of the origin of this behavior has failed to confirm the presence of this bifurcation. Instead, our self-consistency analysis indicates that the symmetric coherent state persists as β decreases but loses stability below $\beta_c \approx 0.7644$, a threshold value that is in good agreement with the numerically determined threshold. At this parameter value a single real eigenvalue passes through zero, becoming positive for $\beta < \beta_c$. The associated eigenfunction is antisymmetric (not shown), indicating that this bifurcation should be a parity-breaking bifurcation leading to drift with a constant speed c that varies with β as $(\beta_c - \beta)^{1/2}$ [34].

To understand why this behavior is not observed we have examined the origin of the oscillations in the speed c. It turns out that these are associated with oscillations in the phase distribution [Fig. 26(a)] localized in the vicinity of a near-discontinuity in the distribution [compare Figs. 24(a) and 24(b)]. The oscillators in this region periodically detrain and entrain, and it is the detraining events that are responsible for the observed episodic drift. We have checked that this is not a discreteness effect: the oscillation frequency at fixed β remains unchanged when N is increased from 512 to 1024 and 2048. However, as one approaches β_c from below these episodes become more and more infrequent and in the vicinity

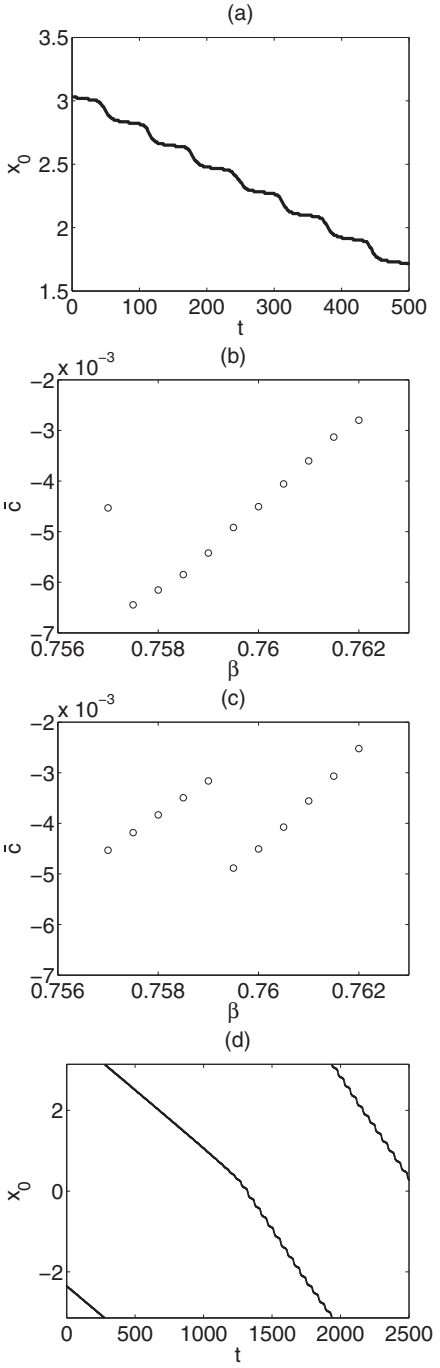

FIG. 25. (a) The position x_0 of the coherent state as a function of time at $\beta = 0.762$. (b) The time-averaged speed $\bar{c}$ of the coherent state as a function of β as β decreases. Note the abrupt decrease in speed at $\beta \approx 0.7570$ associated with the disappearance of the oscillations. (c) The time-averaged speed $\bar{c}$ of the coherent state as a function of β as β increases. Oscillations reappear at $\beta \approx 0.7595$ as shown in (d). The position of the coherent state is measured mod 2π. All calculations are for $N = 512$.

of β_c become nonperiodic. In contrast to the periodic motion, the observed nonperiodic motion is likely a consequence of intrinsic noise in the system whose effects are strongly amplified close to the transition at $\beta = \beta_c$. Indeed, sufficiently near the transition the sign of the phase slip begins to fluctuate

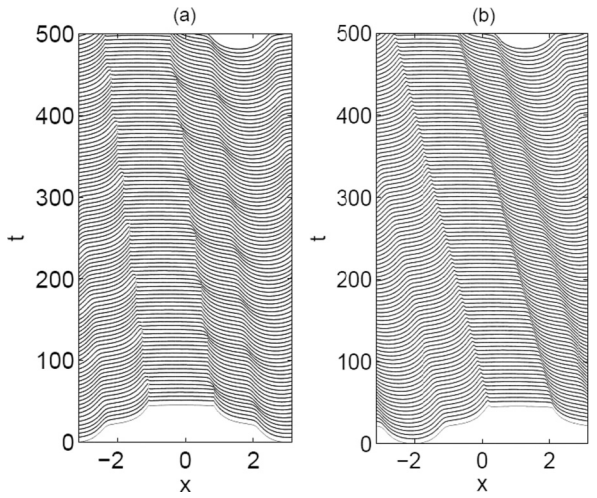

FIG. 26. Hidden line plots of the phase distribution θ as a function of time when (a) $\beta = 0.762$ [oscillatory drift, Fig. 25(a)] and (b) $\beta = 0.755$ (constant drift), both for $N = 512$.

and the coherent state at times shifts to the left but at other times shifts to the right (not shown). Figure 25(b) shows that as β decreases the time-averaged speed $\bar{c}$ increases linearly with decreasing β until $\beta \approx 0.7570$, where there is a hysteretic transition to an oscillation-free drift with a substantially lower speed. Figure 25(c) shows that when β is increased again the system remains in the oscillation-free state until $\beta \approx 0.7595$; at this point the oscillations reappear [Fig. 25(d)] and the speed jumps to a larger value. Evidently the oscillations increase the mean speed because $\bar{c}$ is dominated by the faster motion associated with time intervals corresponding to maximum asymmetry.

We believe that the discrepancy between the linear stability predictions and the observed behavior is a consequence of the fact that the former is based on the smoothed out order parameter Z, which is insensitive to the near-discontinuity in the slope of the phase distribution that appears to be responsible for the instability. For this reason the analysis is unable to capture the imaginary part of the eigenvalue, although it does correctly predict the onset of the instability. Moreover, because the order parameter profile is symmetric the unstable eigenfunction is necessarily antisymmetric, in contrast to the observed unstable mode which is asymmetric but not antisymmetric. For these reasons a consistency analysis of the type used with success for stationary states does not appear to be appropriate for this type of drifting state.

As β decreases further below the hysteresis region the speed c continues to grow linearly but at $\beta \approx 0.646$ the coherent state itself undergoes a hysteretic transition to a stationary two-cluster chimera of the type represented in Fig. 21(a). We have not investigated the origin of this instability in detail.

It turns out that the speed c and the angular frequency Ω of the coherent state can both be computed theoretically and the predictions compared with measured values. For this purpose we suppose that the coherent state is stationary in the moving frame (Fig. 26 indicates that this is at best an approximation); i.e., we suppose that $z(x,t) \equiv u(\xi)$, where $\xi \equiv x - ct$, obtaining a complex nonlinear eigenvalue problem for the speed c and the frequency Ω of the coherent state:

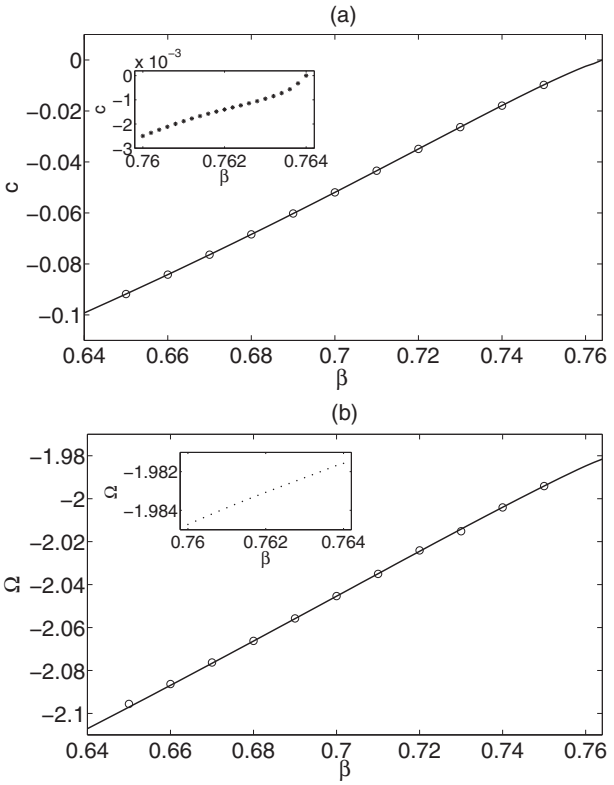

FIG. 27. Comparison of (a) the speed c and (b) the frequency Ω obtained from the solution of the nonlinear eigenvalue problem (36) (solid lines) with measurements computed with $N = 512$ oscillators (open circles), both as a function of β. The inset in (a) reveals the expected square root behavior near $\beta_c \approx 0.7644$. In contrast, the behavior of Ω is approximately linear everywhere.

$$c\tilde{u}_\xi + i\Omega\tilde{u} + \tfrac{1}{2}[e^{-i\alpha}\tilde{U} - \tilde{u}^2 e^{i\alpha}\tilde{U}^*] = 0. \qquad (36)$$

Here $\tilde{u} = u \exp i\Omega t$ and likewise for $\tilde{U}$. This equation is to be solved subject to periodic boundary conditions on $[-\pi,\pi)$. Figure 27 compares the solution of this eigenvalue problem (solid lines) with the measured values (open circles). The agreement is excellent. The inset in Fig. 27(a) shows that sufficiently near β_c the speed c varies as $(\beta_c - \beta)^{1/2}$, as expected of a parity-breaking bifurcation, while Ω is linear in β. Away from this region numerical fits yield $|c| \approx 0.82(\beta_c - \beta)$ and $|\Omega| \approx 1.03(\beta_c - \beta)$. Figure 28 performs a more rigorous test of the two procedures by comparing, for $\beta = 0.66$, the details of the order parameter profiles computed from simulation and from the nonlinear eigenvalue problem. Although the agreement is now less good, it is clear that the nonlinear eigenvalue problem captures the essential details of the order parameter profile and in particular of the asymmetry in the profile that is responsible for the presence of drift. As β increases towards β_c the agreement between the measured and predicted profiles improves dramatically, although a small residual discrepancy remains in regions of near-discontinuity, where the instantaneous profile exhibits localized oscillations [Fig. 24(b)].

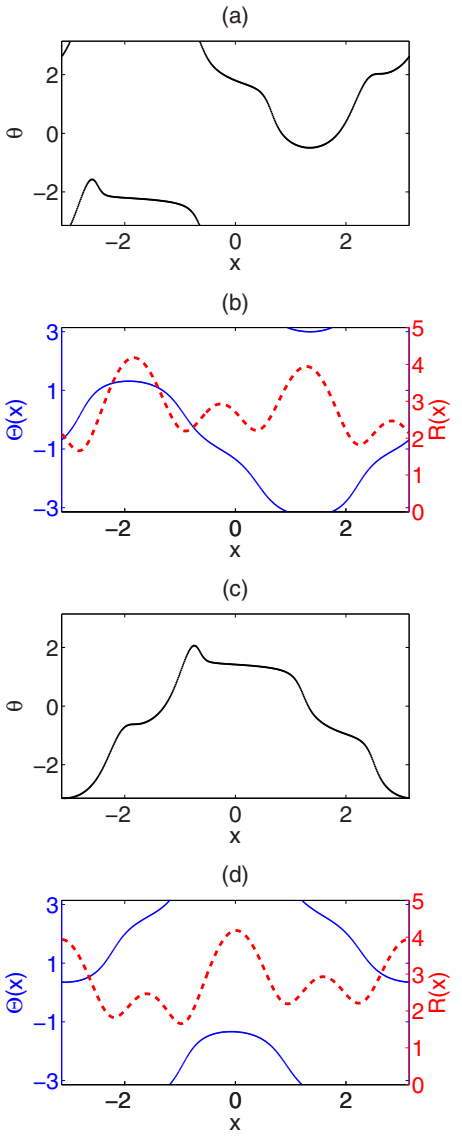

FIG. 28. (Color online) Comparison of the phase and order parameter profiles from direct simulation (top panels) with those obtained from the nonlinear eigenvalue problem when $\beta = 0.66$. The profiles are qualitatively similar modulo translation and overall phase rotation.

D. Traveling chimera states

Apart from the chimera states discussed in the previous subsections, which we consider as stationary in the large N limit, we have also observed one-cluster chimera states in which the coherent cluster drifts at constant speed in the x direction as time evolves. Figure 29 shows a snapshot of such a traveling chimera state when the coupling function is $G_2^{(2)} \equiv \cos(2x) + \cos(3x)$, while Fig. 30 shows examples for $G_3^{(2)} \equiv \cos(3x) + \cos(4x)$. The direction of motion is determined by the gradient of the phase in the coherent region: when the gradient is positive (left panels in Figs. 29 and 30), the cluster travels to the left; when it is negative, it travels to the right. However, the measured speeds are much smaller and in the *opposite* direction from the drift speeds of the $n = 2$ and $n = 3$ (Fig. 29) or $n = 3$ and $n = 4$ (Fig. 30) splay states, whose

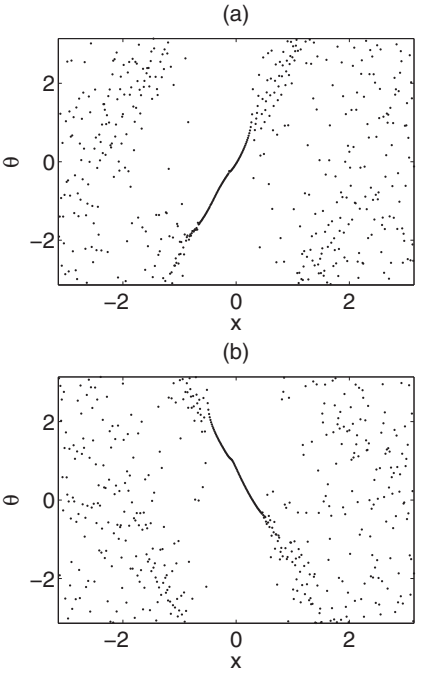

FIG. 29. (a) A left-traveling one-cluster chimera state. (b) A right-traveling one-cluster chimera state. The simulation is done for $\beta = 0.03$ with the coupling $G_2^{(2)} \equiv \cos(2x) + \cos(3x)$ and $N = 512$.

ghostlike signature is evident in the phase distribution in the figures, and in particular in Fig. 31(c). However, despite these differences, the phase gradient in the traveling chimera state with $G_3^{(2)}$ coupling is intermediate between the phase gradients

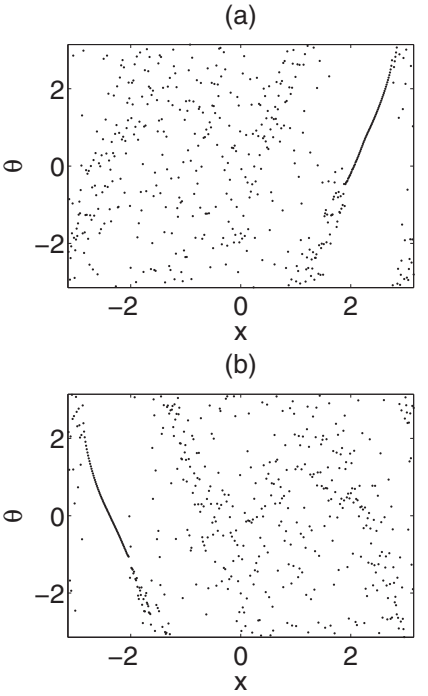

FIG. 30. (a) A left-traveling one-cluster chimera state. (b) A right-traveling one-cluster chimera state. The simulation is done for $\beta = 0.03$ with the coupling $G_3^{(2)} \equiv \cos(3x) + \cos(4x)$ and $N = 512$.

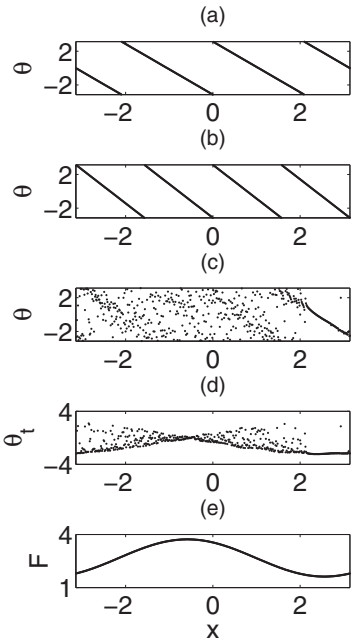

FIG. 31. (a,b) Splay states with $n = 3$ and $n = 4$ for comparison with (c) the traveling chimera state with $G_3^{(2)} \equiv \cos(3x) + \cos(4x)$ coupling. (d) Instantaneous phase velocity of the state in (c). (e) Profile of the function F used to track the position of the coherent structure.

associated with the competing $n = 3$ and $n = 4$ splay states [Figs. 31(a) and 31(b)], and this is so for the $G_2^{(2)}$ coupling as well.

To determine the parameter dependence of the speed of these coherent structures we first need to be able to track their position. As shown in Fig. 31(d), the spatial profile of θ_t at a given instant in time consists of a flat part corresponding to the position of the coherent cluster. Thus the shift in the θ_t pattern provides a unique indication of a shift in the location of the coherent cluster. Following Ref. [21] we pick a reference profile $f(x,x^*) = -\cos(x - x^*)$ and use the value of x^* which minimizes the function

$$F(x^*) := \frac{1}{N}\sum_{k}^{N}[\theta_t - f(x_k,x^*)]^2 \qquad (37)$$

as the position x_0 of the coherent cluster. Figure 31(e) shows a snapshot of the function $F(x^*)$. Figure 32(a) shows the position of the coherent cluster in a periodic domain as a function of time determined using this method when $N = 512$, $\beta = 0.03$. The cluster moves to the right at an almost constant speed $c \approx 0.0077$. Figure 32(b) shows that the speed c is approximately independent of the number N of oscillators, suggesting that the motion is an intrinsic property of the state and not an artifact of the finiteness of N. Finally, Fig. 32(c) shows that the speed c increases with increasing β. As in the case of the stationary chimeras described above, the probability of obtaining a traveling chimera when the simulation starts from random initial conditions decreases as β increases; i.e., the basin of attraction of this state, like those of the stationary states, appears to shrink as β increases.

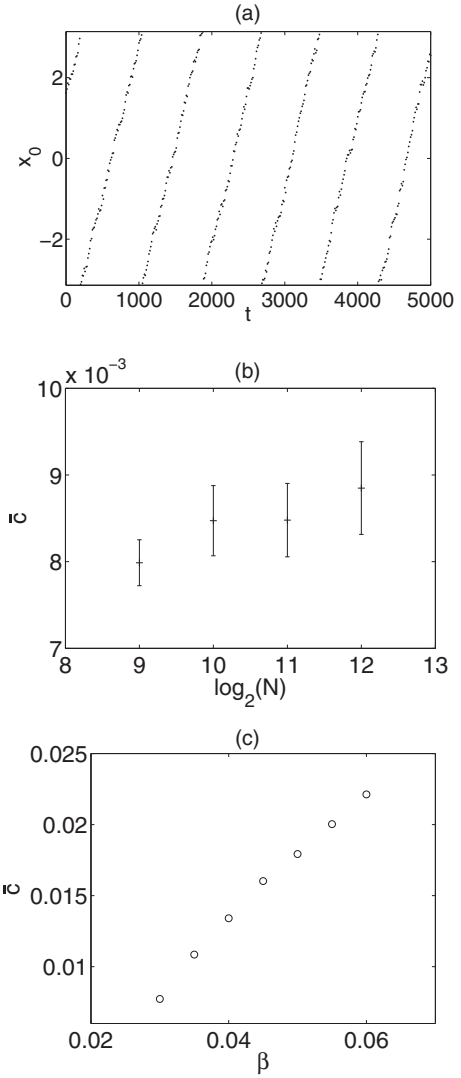

FIG. 32. (a) The position of the coherent cluster as a function of time when $N = 512$, $\beta = 0.03$. (b) The dependence of the time-averaged speed c of the cluster on the oscillator number N when $\beta = 0.03$. (c) The dependence of the time-averaged speed c of the cluster on the parameter β when $N = 512$.

In fact, the traveling chimera state is more complex than suggested by the snapshots in Figs. 29 and 30. This fact is clearly revealed only in a space-time plot of the instantaneous order parameter. Figure 33(a) shows the modulus $R(x,t)$ of the instantaneous local order parameter corresponding to Fig. 30(b), with time increasing upwards. The profile resembles a half-wavelength of a sinusoidal function (Fig. 34) and propagates with approximately constant speed to the right. However, the shape of the profile fluctuates in time, with smaller amplitude waves running on top of the translating bulk profile [Fig. 33(b)].

Altogether we have found for the coupling $G_3^{(2)}$ as many as four distinct stable states: splay states with $n = 3$ and $n = 4$, the stationary multicluster chimera state with seven clusters [Fig. 12(a)], and the one-cluster traveling chimera (Fig. 30). Among these, the splay states are stable for all $0 < \beta < \frac{\pi}{2}$. The multicluster chimera is stable for small β (it is observed

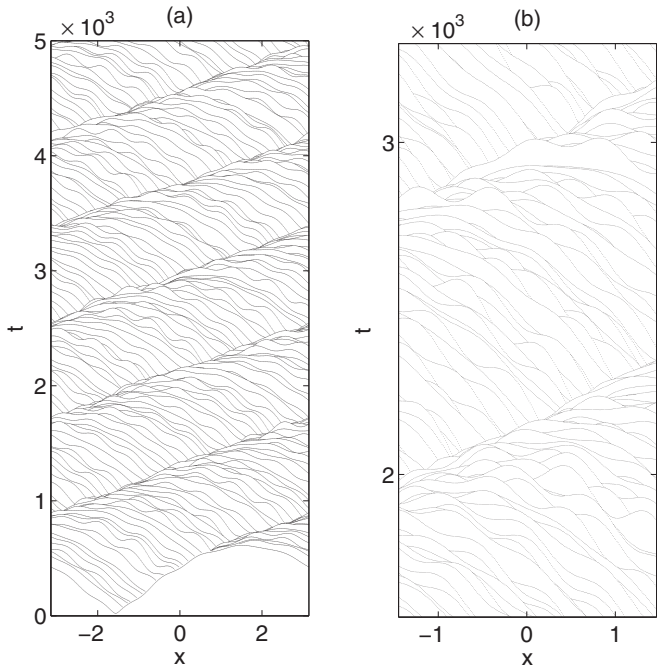

FIG. 33. (a) The local order parameter $R(x,t)$ in a space-time plot for the traveling chimera in Fig. 30(b). (b) Zoom of (a) showing additional detail.

in numerical simulations already when $\beta = 0.001$ although the fraction of the oscillators in the coherent state is then very small). As β increases this state loses stability when β reaches a value between 0.115 and 0.12 and evolves to one or other of the splay states. The traveling chimera is stable in the interval $0.015 \lesssim \beta \lesssim 0.065$; below this range a linear instability takes it to the multicluster state while above this range it takes it into one or other of the splay states. However, despite considerable effort and simulations of very large oscillator systems to get accurate initial conditions, we have not succeeded in solving the corresponding nonlinear eigenvalue problem for the speed c of this state. We attribute this failure to the fact, clearly visible in Fig. 33, that this state does not in fact drift as a rigid object: it is a time-dependent state even in the comoving frame.

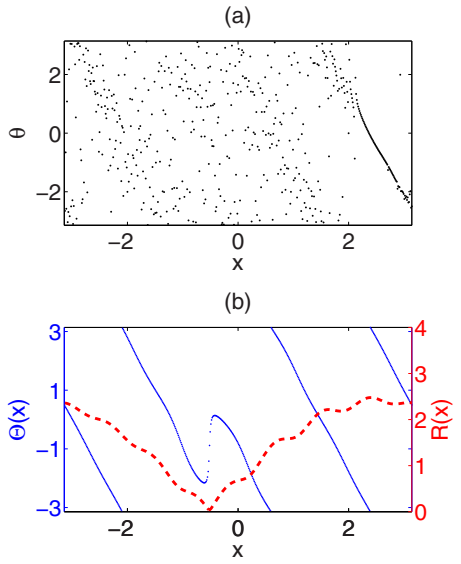

FIG. 34. (Color online) (a) Snapshot of the phase distribution in a one-cluster traveling chimera state with $G_3^{(2)} \equiv \cos(3x) + \cos(4x)$ coupling. (b) Local order parameters R (red dashed line) and Θ (blue dotted line). The simulation is done with $\beta = 0.03$ and $N = 512$.

IV. CONCLUSION

In this paper we have investigated the effects of nonlocal coupling of indefinite sign on a system of identical phase-coupled oscillators. We focused on the case with positive (attractive) coupling over small distances and negative (repulsive) coupling over large distances, as exemplified by the coupling functions $G_n^{(1)} \equiv \cos(nx)$ and $G_n^{(2)} \equiv \cos(nx) + \cos[(n+1)x]$, and identified a variety of evenly spaced stationary multicluster chimera states without having to rely on the presence of time delay or parameter heterogeneity [19,23,24]. More significantly, we also found a class of chimeras with uneven separation, traveling coherent states, and a traveling chimera state. In contrast to the earlier systems referred to above the chimera states in the system studied here have relatively large basins of attraction and no specially tailored initial conditions are required to obtain such states. In particular, robust chimeras are realized starting from random initial conditions.

We have given a fairly complete description of the different accessible states using a self-consistency analysis based on Eq. (12) and showed that this type of analysis works well not only for stationary evenly spaced chimeras but also for the exotic unevenly spaced chimeras. In particular, we were able to show that the local order parameter profiles predicted by this type of analysis agree well with the phase distribution generated in direct numerical simulations of the coupled oscillator system. We used these results to make predictions for different types of transitions that these states may undergo, merger of coherent clusters and transition to a drifting state, and confirmed these predictions using numerical simulations. The self-consistency analysis predicted instability thresholds accurately but missed some crucial details, including the presence of localized small amplitude oscillations near the onset of the drift instability. Despite this failure the drift speed predicted from the solution of a nonlinear eigenvalue problem obtained from the self-consistency analysis was in excellent agreement with the numerically determined speed, and likewise for the overall rotation frequency Ω of the phase distribution. Stable (nonsplay) traveling states appear to require a significant contribution from both n and $n+1$ modes in the coupling function $G_n^{(2)}$. We have checked, for example, that with $G(x) = \cos(3x) + A\cos(4x)$ the traveling chimera present at $A = 1$ loses stability when $A \approx 0.95$; when this occurs the system evolves to a traveling splay state instead. However, we were unable to obtain an analytical description of the traveling chimera state and its stability properties.

It is of considerable interest to see to what extent the results from the system studied here carry over to more realistic oscillator systems, such as those studied in Refs. [35–38],

when these are coupled nonlocally with an attractive-repulsive coupling. We plan to report on these questions in future work.

ACKNOWLEDGMENT

This work was supported in part by a National Science Foundation Collaborative Research Grant CMMI-1232902.

[1] A. T. Winfree, *The Geometry of Biological Time* (Springer, New York, 1980).
[2] Y. Kuramoto, *Chemical Oscillations, Waves, and Turbulence* (Springer, New York, 1984).
[3] M. Nixon, M. Friedman, E. Ronen, A. A. Friesem, N. Davidson, and I. Kanter, Phys. Rev. Lett. **108**, 214101 (2012).
[4] S. H. Strogatz and R. E. Mirollo, Phys. Rev. E **47**, 220 (1993).
[5] R. E. Mirollo and S. H. Strogatz, SIAM J. Appl. Math. **50**, 1645 (1990).
[6] I. G. Malkin, *Methods of Poincare and Liapunov in Theory of Non-linear Oscillations* (Gostexizdat, Moscow, 1949) [in Russian, *Metodi Puankare i Liapunova v Teorii Nelineinix Kolebanii* (Gostexizdat, Moscow, 1949)].
[7] Y. Kuramoto, Prog. Theoret. Phys. Suppl. **79**, 223 (1984).
[8] J. D. Crawford, J. Stat. Phys. **74**, 1047 (1994).
[9] S. H. Strogatz, Physica D **143**, 1 (2000).
[10] J. A. Acebron, L. L. Bonilla, C. J. P. Vicente, F. Ritort, and R. Spigler, Rev. Mod. Phys. **77**, 137 (2005).
[11] D. A. Wiley, S. H. Strogatz, and M. Girvan, Chaos **16**, 015103 (2006).
[12] Y. Kuramoto and D. Battogtokh, Nonlinear Phenom. Complex Syst. **5**, 380 (2002).
[13] D. M. Abrams and S. H. Strogatz, Phys. Rev. Lett. **93**, 174102 (2004).
[14] A. Prigent, G. Grégoire, H. Chaté, O. Dauchot, and W. van Saarloos, Phys. Rev. Lett. **89**, 014501 (2002).
[15] A. Prigent, G. Grégoire, H. Chaté, and O. Dauchot, Physica D **174**, 100 (2003).
[16] D. Barkley and L. S. Tuckerman, Phys. Rev. Lett. **94**, 014502 (2005).
[17] D. M. Abrams and S. H. Strogatz, Int. J. Bifur. Chaos Appl. Sci. Eng. **16**, 21 (2006).
[18] D. M. Abrams, R. Mirollo, S. H. Strogatz, and D. A. Wiley, Phys. Rev. Lett. **101**, 084103 (2008).
[19] G. C. Sethia, A. Sen, and F. M. Atay, Phys. Rev. Lett. **100**, 144102 (2008).
[20] C. R. Laing, Chaos **19**, 013113 (2009).
[21] O. E. Omel'chenko, M. Wolfrum, and Y. L. Maistrenko, Phys. Rev. E **81**, 065201 (2010).
[22] C. R. Laing, K. Rajendran, and I. G. Kevrekidis, Chaos **22**, 013132 (2012).
[23] Y. Zhu, Y. Li, M. Zhang, and J. Yang, Europhys. Lett. **97**, 10009 (2012).
[24] S. R. Ujjwal and R. Ramaswamy, Phys. Rev. E **88**, 032902 (2013).
[25] O. E. Omel'chenko, Nonlinearity **26**, 2469 (2013).
[26] G. D. Ermentrout and D. H. Terman, *Mathematical Foundations of Neuroscience* (Springer, New York, 2010).
[27] M. Wolfrum, O. E. Omel'chenko, S. Yanchuk, and Y. L. Maistrenko, Chaos **21**, 013112 (2011).
[28] O. E. Omel'chenko, M. Wolfrum, and C. R. Laing, Chaos **24**, 023102 (2014).
[29] G. Bordyugov, A. Pikovsky, and M. Rosenblum, Phys. Rev. E **82**, 035205(R) (2010).
[30] A. Pikovsky and M. Rosenblum, Phys. Rev. Lett. **101**, 264103 (2008).
[31] C. R. Laing, Physica D **238**, 1569 (2009).
[32] E. Ott and T. M. Antonsen, Chaos **18**, 037113 (2008).
[33] S. H. Strogatz, *Nonlinear Dynamics and Chaos* (Addison-Wesley, Reading, MA, 1994).
[34] P. Coullet, R. E. Goldstein, and G. H. Gunaratne, Phys. Rev. Lett. **63**, 1954 (1989).
[35] H. Sakaguchi, Phys. Rev. E **73**, 031907 (2006).
[36] C. R. Laing, Phys. Rev. E **81**, 066221 (2010).
[37] I. Omel'chenko, O. E. Omel'chenko, P. Hövel, and E. Schöll, Phys. Rev. Lett. **110**, 224101 (2013).
[38] G. C. Sethia and A. Sen, Phys. Rev. Lett. **112**, 144101 (2014).